Volume 30 | Number 3 | March 2015 | Pages 529–840

# JAAS

Journal of Analytical Atomic Spectrometry

www.rsc.org/jaas

## Themed issue: Synchrotron radiation and neutrons in art and archaeology 2014

ISSN 0267-9477

ROYAL SOCIETY OF CHEMISTRY

PAPER

Claire Gervais *et al.*

Degradation mechanisms of reinforcing iron rebars in monuments: the role of multiscale porosity in the formation of corrosion products investigated by X-ray tomography

JAAS

PAPER

Cite this: *J. Anal. At. Spectrom.*, 2015, **30**, 580

# Degradation mechanisms of reinforcing iron rebars in monuments: the role of multiscale porosity in the formation of corrosion products investigated by X-ray tomography

Mathieu Jacot-Guillarmod,[a] Olivier Rozenbaum,[b] Valérie L'Hostis,[c] Philippe Dillmann,[c] Delphine Neff[c] and Claire Gervais*[a]

Received 31st October 2014
Accepted 13th January 2015

DOI: 10.1039/c4ja00388h

www.rsc.org/jaas

Monuments in stone often contain metallic reinforcements, the stability and degradation state of which determines the entire integrity of the edifice. Understanding their long-term corrosion process is thus an essential step towards a safe and efficient conservation strategy. In this study, we show that combining laboratory and synchrotron tomography at different scales is efficient for getting an overall three-dimensional picture of the iron corrosion products found in iron rebars from Orléans cathedral. We demonstrate that beside chemical characterization of the corrosion products, the study of the shape of the corrosion products, their spatial distribution within the stone binder and their relationship with the porosity of the binder can bring significant insights into the corrosion process, and particularly help in understanding the multiple roles that porosity plays in corrosion.

## 1 Introduction

Gothic cathedrals have been built, thanks to metallic reinforcement, metallic chains and rebars. These elements can be embedded in lime, mortar or hydraulic binders and corrode in contact with these media.[1] The mechanical resistance of the metallic elements is affected by the corrosion processes, endangering the edifice.[2,3] In order to assess the possible damage and establish a reliable conservation diagnosis, a thorough knowledge of the corrosion mechanisms is thus required.[4,5] The corrosion part can be schematically described by the presence of a corrosion layer constituted of iron oxide and oxyhydroxides called the dense product layer (DPL) and a mixed zone called the transformed medium (TM), in which iron is heterogeneously distributed within the binder.[6–8] Particularly in the case of cementitious or hydraulic binders, the TM presents a multiscale porosity network partially filled with the corrosion products. Radial cracks spreading out from the metallic core may also be found, sometimes filled with corrosion products as well.

While the TM is well characterized, little is known on its formation process, *i.e.* how corrosion products built up within the binder. Understanding this process would help to predict the long-term corrosion of iron embedded in mortars. This in turn would help to estimate which monuments are sensitive to corrosion and need to be particularly controlled.

In this paper, we tackle this issue by investigating the relationship between porosity and corrosion products within the binder. For this purpose, corroded bars from the north tower of Orléans cathedral dated from the XVIII$^{th}$ century were chemically characterized and investigated by laboratory and synchrotron micro X-ray tomography.[9,10] By means of adequate image processing and quantitative analysis tools, we characterized the shape and spatial distribution of porosity and iron within the TM, as well as their complex, dynamical relationships. Based on these results, we discuss a general scenario that describes the formation of corrosion products for iron materials embedded in mortars.

## 2 Materials and methods

### Sample preparation

The iron corroded rebars from the north tower of Orléans cathedral were investigated. The bars are embedded in limestone and are sealed with a white binder. Samples were extracted from the bars so that the entire corrosion system (metallic core + DPL + TM) could be investigated. The characterization of the corrosion system was carried out on cross-sections for the chemical analyses and on matchsticks of 2 × 2 mm$^2$ sections realized at the interface between DPL and TM for X-ray-tomography (Fig. 1). Cross sections and matchsticks were prepared as follows: the sample was first embedded in epoxy

[a]*Bern University of the Arts, Fellerstrasse 11, CH-3027 Bern, Switzerland. E-mail: claire.gervais@bfh.ch*

[b]*Univ. Orléans, CNRS, BRGM, ISTO, UMR 7327, BP 36009, 45071, Orléans 45060, France*

[c]*LAPA: NIMBE SIS2M UMR3299 CEA/CNRS and IRAMAT UMR5060 CNRS, CEA Saclay, 91191 Gif sur Yevtte Cedex, France*

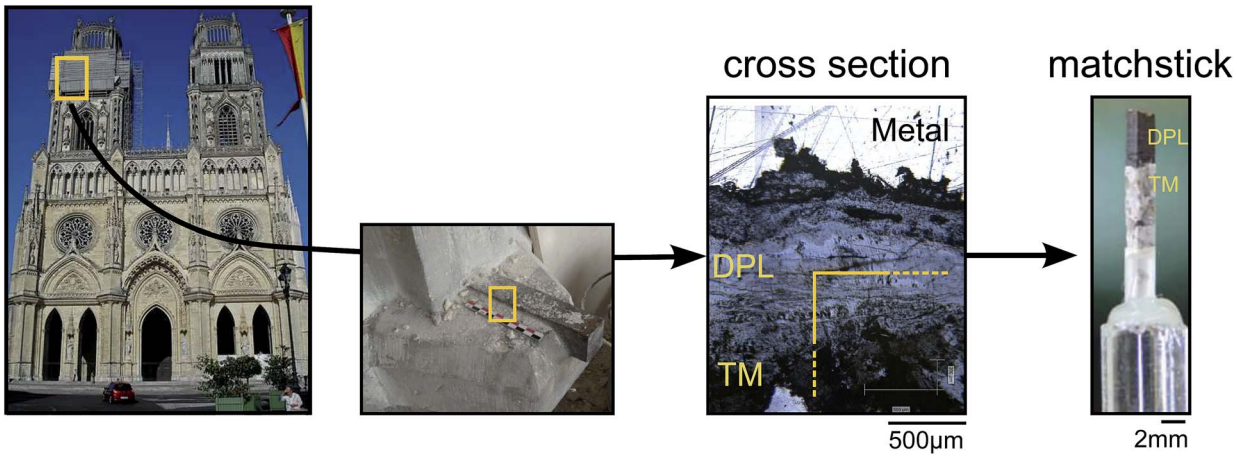


Fig. 1 Sample preparation of iron rebars from Orléans cathedral (France). Chemical analysis was performed on cross-sections and X-ray tomography on matchsticks. Yellow regions indicate regions of study.

resin at room temperature in order to consolidate it and prevent loss from the brittle corroded regions. The cross-sections were then cut and prepared according to the metallographic standard: the surface was ground with SiC papers from grad 80 to 4000 and then was polished with diamond paste down to 1 µm. Ethanol was used as a lubricant during this preparation, in order to avoid any phase dissolution. Further matchstick samples were prepared from the cross-sections. For this purpose, the latter were again embedded in epoxy resin and a slice of 2 mm was cut with a precision saw equipped with a diamond wheel. The 2 mm-slice was embedded in epoxy resin once more before being cut on its edge to obtain a $2 \times 2$ mm$^2$ matchstick.

The characterization of the morphology, composition and crystalline structure of the corrosion products was performed, thanks to optical and scanning electron microscopes (OM and SEM at 15 kV), energy dispersive spectroscopy (EDS, Si(Li) detector equipped with a Be window) and Raman spectroscopy (at 532 nm). These microbeam techniques delivered complementary information on various parts of the system. The analytical protocol has been extensively described in ref. 8.

### Laboratory X-ray microtomography

Microtomography analyses were first performed using a laboratory-based computed tomography (CT) device Nanotom 180NF (GE Phoenix—X-ray, Wunstorf, Germany). This unit has a 180 kV nanofocus X-ray tube emitting a conical beam and a digital detector array (2304 × 1152 pixels Hamamatsu detector). In order to obtain high penetrating X-rays, a target made of tungsten was selected and an operating voltage of 160 kV with a filament current of 23 µA was applied. The matchsticks were mounted and waxed on a carbon fiber rod, so that their axial direction ($z$, hereafter) was parallel to the axis of rotation. They were then placed in the acquisition chamber and rotated at 360 degrees during acquisition. The distance between the X-ray source and the sample and between the X-ray source and the detector was 47 mm and 500 mm, respectively, giving a voxel size of 4 µm. The 720 projection images (angular increment of 0.5°) were acquired during sample rotation (acquisition time: 33 minutes). The resulting projections were converted into a 3D image stack using the Phoenix 3D reconstruction software based on the filtered back projection Feldkamp algorithm.[11]

### Synchrotron X-ray microtomography

The synchrotron microtomographic images were collected at the ID19 beamline of the European Synchrotron Radiation Facility (ESRF, Grenoble, France). A pink beam with a maximum intensity centered around 65 keV was used. The matchsticks were imaged with phase-contrast and a 0.7 µm voxel size. A local tomography protocol was used to obtain this high resolution without further cutting the brittle matchsticks. Successive rotations of the sample, 3000 projections, corresponding to 3000 angular positions ranging between 0 and 180, were acquired using a 2048 × 2048 pixels FReLoN CCD camera (acquisition time: 7 minutes). The samples were mounted on a vertical rotator on a goniometric cradle. An efficient filtered back-projection algorithm adapted for local tomography applications (PyHST software, ESRF) was used for the reconstruction.[12]

## 3 Results

### 3.1 Chemical characterization of samples

As observed on the SEM image of Fig. 2, the DPL has a thickness between 800 µm and 1.1 mm. Raman spectroscopy indicates that the corrosion products are mainly goethite, with light marblings composed of magnetite and maghemite. SEM-EDS analysis shows that the binder is constituted of millimetric grains (binder grains) composed mainly of Si, K and Al, and identified principally as quartz. Those grains are included in a Ca-rich matrix (binder matrix). A porosity network is observed in the dark in the SEM image. Fe is present in the DPL and also around the grains in the TM. In the Fe-rich zones of the TM, we observe a significantly lower Ca concentration. These observations are similar to those given in the literature.[6,8]

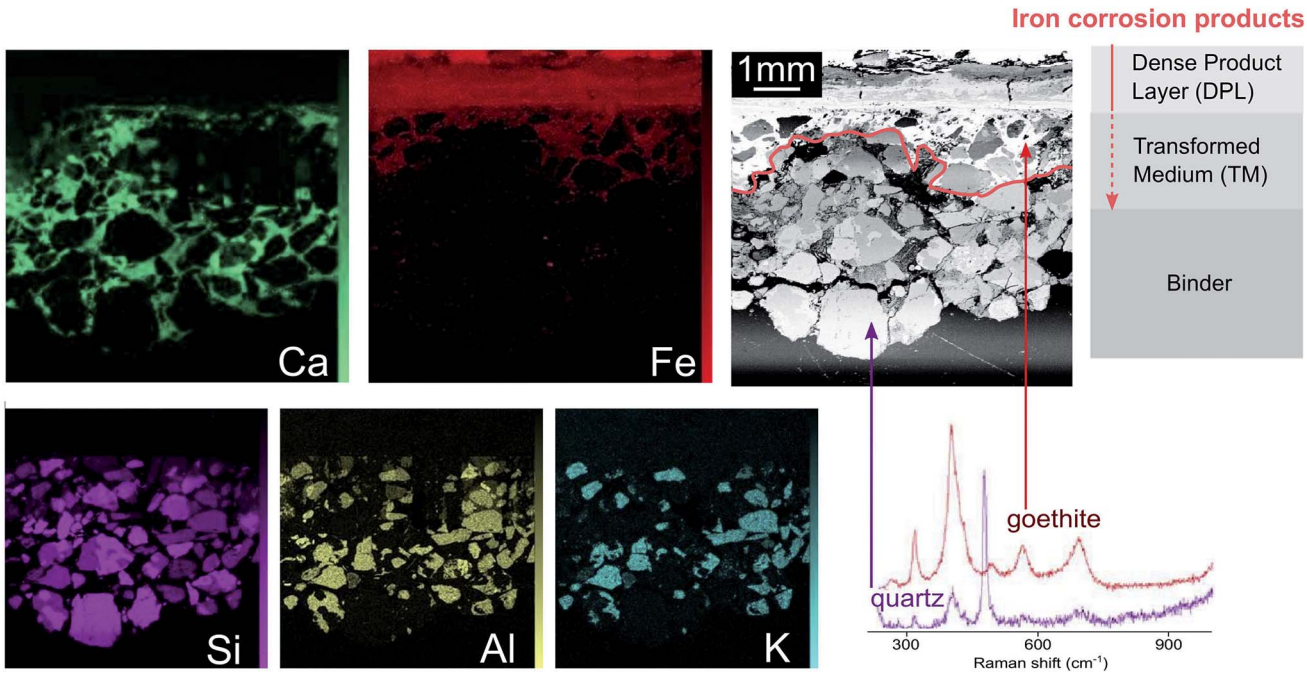


Fig. 2 Chemical characterization of iron corrosion products and binders by means of SEM-EDS and Raman spectroscopy.

### 3.2 Segmentation of laboratory CT images

The distribution of the corrosion products precipitated in the TM and their connectivity to the porosity network of the binder were further investigated by X-ray tomography. Because the sample is inherently heterogeneous, it was first visualized by laboratory X-ray tomography with a large field of view (4.5 × 4.5 mm) and medium resolution (voxel size 4 μm), in order to get the largest and most representative overview of the TM (Fig. 3).

According to the X-ray attenuation coefficients of the main elements present in the sample, and in relationship with the chemical analysis previously performed, we could identify three sets of greyscale values that were used as a basis for further segmentation: *Iron*: high grey levels corresponding to the iron corroded phases and iron-rich phases naturally present in the cement; *Binder*: medium grey levels corresponding to the binder grains and Ca-rich binder matrix; and *Porosity*: low grey levels including porosity and embedding resin. These three sets are distributed within the three regions that characterize these types of corroded materials: (1) the DPL region composed of corroded iron phases, (2) the TM region, where the precipitated iron corrosion phases coexist with the binder and (3) the cementitious binder mainly composed of binder quartz grains, binder matrix, porosity and a few but well-identified iron-containing minerals.

The raw CT images are not directly suitable for segmentation into the three sets *Iron*, *Binder* and *Porosity*. Measurement artefacts such as beam hardening effects, intensity rings caused by temporary and spurious bad pixels in the detector, and noise, must be filtered out before segmentation. We chose to apply the inverse scale space filter (ISS) based on the ROF model (Rudin–Osher–Fatemi),[13–15] because it was efficient in removing noise while keeping the edges well-defined (Fig. 4). After filtering, we segmented the images with an in-house algorithm adapted from Otsu's method.[16] In the original method developed by Otsu, the segmentation between two sets is done by calculating

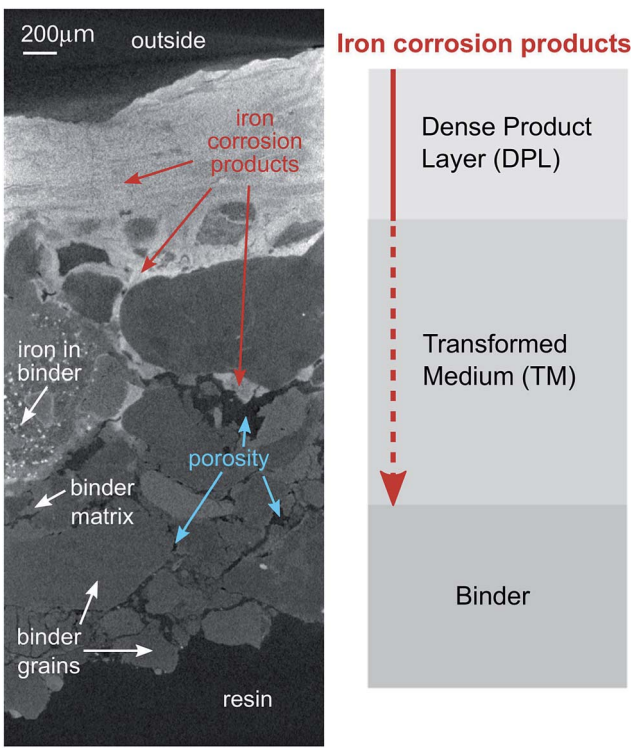


Fig. 3 Cross-section along the main direction (*z*) of the sample showing the distribution of the iron corrosion products and porosity within the Dense Product Layer (DPL), Transformed Medium (TM) and binder. TM is defined as the region containing precipitated corrosion products within the binder.

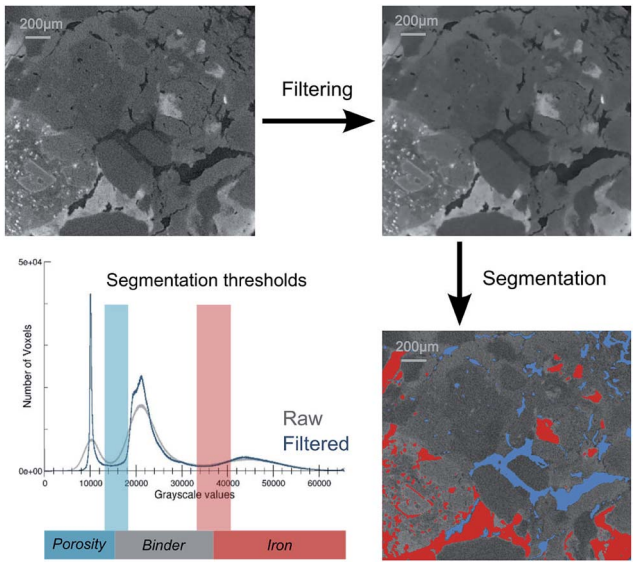


Fig. 4 Filtering-segmentation procedure applied to raw laboratory CT images before analysis (here, *xy* cross-section represented). For the segmented image, the set *Porosity* is colored in blue, *Iron* in red, and *Binder* is left in grayscale for clarity. Below: distribution of grayscale values in the entire sample, before and after filtering. The range of local grayscale thresholds used for the segmentation of the three sets are [13 424–18 264] and [33 152–41 328] for *Porosity–Binder* and *Binder–Iron*, respectively.

a grayscale threshold that divides the grayscale distribution of the entire sample into two classes. Voxels are then attributed to the segmented set according to the class to which their grayscale value belongs. The threshold is determined by maximizing the variance between the classes and minimizing the variance within the classes. When more than two sets must be segmented, the classes determined previously are further divided into sub-classes by the same thresholding procedure.

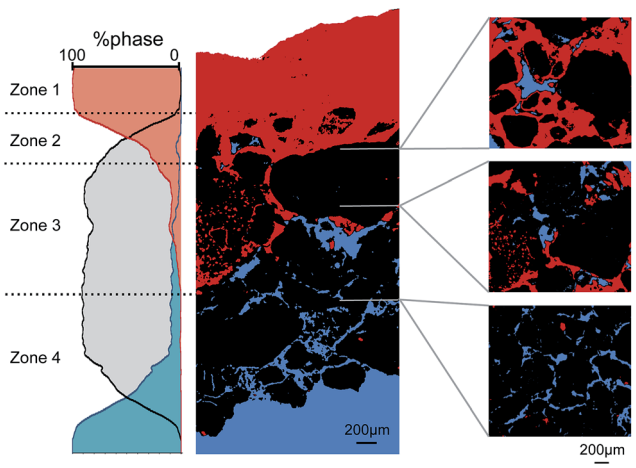


Fig. 5 Visualization of *Iron* and *Porosity* along the *z* direction and within (*xy*) sections. *Porosity* is colored in blue, *Iron* in red, and *Binder* in black. The graph on the left represents the relative distribution of the three segmented sets along the *z* direction.

In our case, we could not apply directly Otsu's method on the entire sample, because of measurement artefacts leading to an overall shift of the grayscale values, from the center to the edge of the sample. This intensity inhomogeneity is likely due to beam hardening and it cannot be easily overcome during reconstruction or by filtering. It is also non-linear, so that it could not be removed artificially by, for instance, applying a correction function to the grayscale values according to their position in the sample. To circumvent this issue, we modified Otsu's method in such a way that it is not applied to the entire sample, but locally. The exact procedure will be detailed somewhere else. In short, it consists of sectioning the sample into about 6000 separate regions. For each region, a list of thresholds is estimated based on the local grayscale histogram. The threshold of each voxel is computed by a linear combination of the region's thresholds weighted by the distance of the voxel to the center of the regions. This ensures continuity in the segmentation, even between regions. With this procedure, we could obtain correctly segmented images, despite the intensity inhomogeneity. The *Iron* and *Porosity* sets were well segmented, including those in regions difficult to grasp computationally (see for instance the bottom left of the segmented image in Fig. 4).

### 3.3 Characterization of *Iron* and *Porosity* networks in laboratory CT images

The simplest characterization of the segmented sets consists of a visualization of their size, shape, and location within the sample (Fig. 5). They are sequentially located along the *z* direction of the sample. At the top, *Iron* is composed of corrosion products corresponding to the DPL (Zone 1). Close to the DPL, *Iron* further spreads into the TM like an iron mold covering part of the grains of the binder (Zone 2). In this zone, the binder grains look more spread apart from each other and rounder than in the rest of the sample. More deeply into the TM (Zone 3), *Iron* evolves around the grains of the binder, with a shape following that of the porosity. Note for instance the continuity between the *Iron* and *Porosity* networks around the large binder grain in the middle of the *z* cross-section. In this zone too, *Iron* is dispersed into tiny clusters, such as those on the left side of *z* cross-section. With the help of Fig. 4, we can label those tiny clusters as iron-bearing minerals present in the original binder (and not as iron corrosion products). Finally, the bottom of the sample contains the raw binder phase, free from corrosion products, defined by grains packed together and porosity in between (Zone 4).

The connectivity of the segmented sets *Iron* and *Porosity* was analyzed by separating further the sets into clusters. Clusters contain voxels that belong to the same set and that are connected with each others by sharing common faces. We used the Hoshen–Kopelman algorithm for that purpose,[17] which efficiently computes large data sample sets such as ours ($\approx 2.6 \times 10^8$ voxels) (Table 1).

Both *Iron* and *Porosity* are composed of a very large cluster accounting for 97.8% and 96% of the total volume, respectively. Those mega-clusters are percolating, that is they are connected to

Table 1 Frequency of clusters ranged according to their size $S$. Mega-clusters: $S > 10^6$ voxels; kilo-clusters: $10^3 < S \leq 10^6$; small clusters: $S \leq 10^3$

| | *Iron* | *Porosity* |
|---|---|---|
| Mega-clusters (% total phase) | 1 (97.8) | 1 (96.0) |
| Kilo-clusters (% total phase) | 113 (1.9) | 156 (3.3) |
| Small clusters (% total phase) | 2579 (0.4) | 4628 (0.7) |

each other and cross the sample from end to end. Thus, a water molecule coming from the outside of the sample could wander through the main cluster of porosity and eventually come into contact with the *Iron* set and the corroded products composing it.

Beyond a visual evaluation of the segmented sets and with the aim of quantifying their shape, we employed topological tools and calculated the Betti numbers of *Iron* and *Porosity* mega-clusters. In algebra, Betti numbers are used to characterize and distinguish topological surfaces. Roughly speaking, the Betti number $\beta_n$ is a measure of the number of holes in $n$-dimensions. $\beta_1$ refers to the number of one-dimensional (1D) holes, while $\beta_2$ accounts for two-dimensional holes, which could be translated by "closed cavities" in plain English. For instance, a tennis ball is an object with $\beta_1 = 0$ and $\beta_2 = 1$, because it has a spherical cavity within it, *non accessible from the outside*. In contrast, a wedding ring is an object with $\beta_1 = 1$ as it has a hole to wear it on the finger, but $\beta_2 = 0$ because no closed cavity can be found. As shown in Table 2, Betti numbers differ significantly between *Iron* and *Porosity* main clusters: *Iron* features both 1D holes (1686) and closed cavities (1291), in contrast to *Porosity* that predominantly has 1D holes (3274). Comparatively, *Porosity* contains more holes and cavities than *Iron* (compare normalized values 78 + 6 with 26 + 20). In other words, the *Iron* mega-cluster is bubbly and less jagged than the *Porosity* mega-cluster.

### 3.4 Microscale visualization of iron corrosion products interfaced with binder and porosity on synchrotron CT images

While CT images with medium resolution but a large field of view are necessary to get a representative picture of the distribution and shape of the phases within the samples, it is just as necessary to work on CT images with higher resolution, in order to investigate the specificities of the corrosion products and their interface with binder and porosity in more detail. A region of the TM (corresponding to Zone 2 in Fig. 5) was thus visualized on a second sample by phase-contrast synchrotron X-ray tomography, resulting in CT images with a 0.7 μm voxel size.

The corrosion products exhibit a variety of shapes and crystalline states. For instance, they are found in the form of needles within interstices of binder grains (Fig. 6).

When in contact with porosity, the corrosion products have a more regular pattern, and their crystallinity evolves with their location in the corrosion layer (Fig. 7). Deep into the TM, the iron corrosion products are highly porous (1) and present a smooth interface with porosity. Closer to the DPL, the interface between iron corrosion products and porosity presents more distinct crenels, and a slight variation of the grayscale suggest a variable local density of the phases (2 and 3). Note the presence of margins constituted of successive strata at the interface between the corrosion products and the porosity on images 2, 3 and 4. They could be due to a change in the local chemical conditions (Eh, pH, iron concentration…) inducing either a local change of the type of phase precipitated, or a variation for the same phase of its crystallinity or density among different strata. Even closer to the DPL, we observe a more differentiated interface between iron corrosion phases and porosity, with distinct layers (4) and well-crystallized iron corrosion products with whisker-shapes (4 and 5). Finally, close to the DPL, those whiskers are predominant and may fill entire areas (6). The evolution presented here was found in other places of the sample and can be summarized as follows: the closer to the DPL, the higher crystalline with well-defined crystals, principally whiskers. The deeper in the binding medium, the less crystalline and the more microporous are the iron corrosion products.

## 4 Discussion

Metallic objects embedded within a mortar undergo a corrosion process in an unsaturated medium. Corrosive elements from the outside (such as oxygen) are transported at the beginning of the corrosion period at the metallic surface through the porous

Table 2 Betti numbers calculated for *Iron* and *Porosity* mega-clusters. To compare, numbers have been normalized by the cluster size ($\times 10^6$ voxels). Images show holes (H) found in the *Porosity* mega-cluster and cavities (C) found in the *Iron* mega-cluster

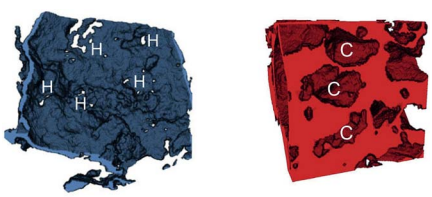


| | Holes ($\beta_1$) | Cavities ($\beta_2$) |
|---|---|---|
| *Iron* (norm.) | 1686 (26) | 1291 (20) |
| *Porosity* (norm.) | 3274 (78) | 265 (6) |

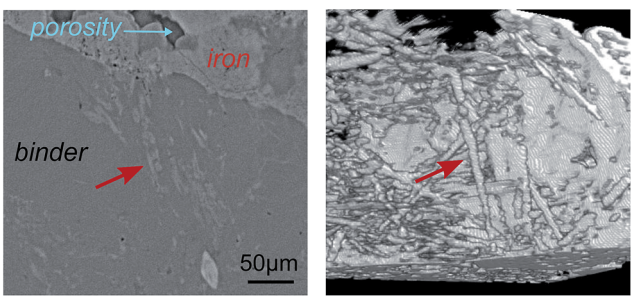


Fig. 6 Presence of iron corroded products within interstices of a binder grain visible on synchrotron CT images. Left: 2D cross-section; right: 3D visualization of the iron corrosion products (white) isolated from the rest of the sample. The 2D and 3D views are of the same region of the sample (red arrow used as a guideline).

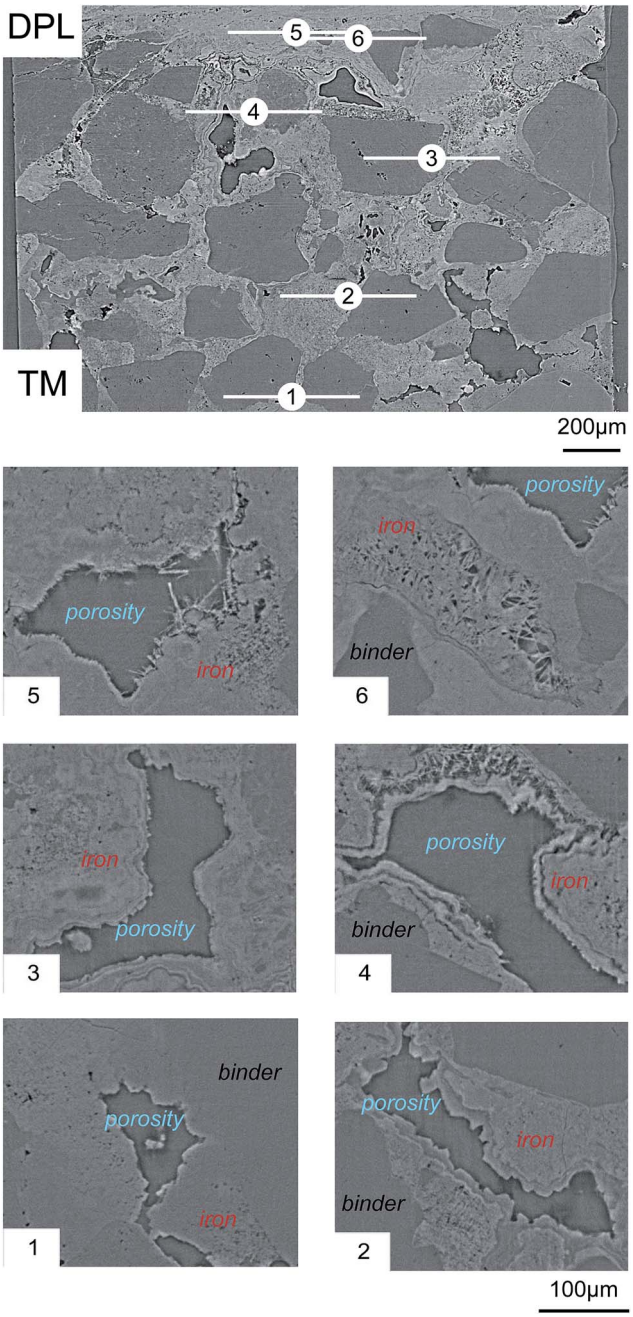


Fig. 7 Synchrotron CT images showing the gradual degree of crystallization (whiskers) of the iron corrosion products in the vicinity of porosity. Top: *xz* cross-section showing DPL at the top and the TM at the bottom of the sample. Bottom: *xy* cross-sections showing iron corrosion products in the vicinity of closed pores in several regions of the sample (indicated as 1–6 on the top image).

network of the binder. Corrosion starts when the carbonatation process induces a decrease of the local pH near the metallic element after the transformation of the binder.[18] Ferrous ions form, migrate and precipitate as corrosion products, following the local chemical conditions. Our observations suggest that this precipitation principally takes place *within* the sub-milliporosity naturally present around the grain binders, but extends also *beyond*, within regions initially occupied by the binder.

The iron corrosion products and the porosity share a similar overall appearance (they are both tortuous, highly connected and naturally surrounding the binder grains) and a clear continuity exists between their networks (Fig. 5, Zone 3). Besides, closed porosity cavities surrounded by corrosion products are present in the vicinity of the DPL. All these facts support a scenario presenting the sub-milliporosity of the binder as the primary region where iron precipitation occurs: the dissolved iron migrates within the porosity network of the binder, precipitates at the surface of the binder grains and thus gradually fills the binder's porosity. Hardly reachable parts of this porosity are eventually cut from the rest of the porosity by the precipitated iron corrosion products, and remains in the sample as non-accessible voids.

Beyond the sub-milliporosity of the binder, there are other regions where precipitation of iron corrosion products occurs, such as micro-cracks and interstices within the binder grains (Fig. 6). It is not clear whether these cracks were present originally or they were created by the mechanical pressure resulting from the precipitation process. This last option cannot be ruled out, as corrosion products have a low-density (*e.g.* goethite = 4.2 g $cm^{-3}$ compared to iron = 7.8 g $cm^{-3}$) and thus require a significant volume to precipitate.

Another region which could be also involved in the precipitation of iron corrosion products is the Ca-rich binder matrix, nanoporous by essence. Indeed, it is puzzling to see that Zone 2 is composed principally of iron corrosion products, closed cavities of porosity and a binder uniquely composed of binder grains (Fig. 7). No light grayscale zones associated with a Ca-rich binder in comparison with the EDS images could be clearly identified in the CT images in this region. Could this absence be due to the precipitation of iron *within* the nanoporous binder matrix? On the CT images, this would result in partial volume effects, with voxels composed of a mixture of nanoporous precipitated iron corrosion products and the binder matrix. These voxels would still be segmented as being *Iron*, hence leading to the composition of Zone 2 we observe (with *Iron* and *Binder* grains only). However, the grayscale values of these mixed voxels should be slightly lower than voxels containing plain corrosion phases because of the low-attenuation coefficient of calcium. We thus computed the average greyscale values of the voxels segmented as *Iron* as a function of their location within the sample (Fig. 8).

The results clearly indicate that *Iron* voxels in Zone 2 have the same greyscale values as *Iron* voxels in the DPL (Zone 1). Therefore, the fact that no Ca-rich binder matrix is observed in Zone 2 cannot be explained by a mixture between the iron corrosion products and the binder matrix. Rather, it is more probable that no or much less cement (*i.e.* binder matrix) was present initially at the interface between the rebar and the binder.

The situation is different in Zone 3, where the mean greyscale value of *Iron* voxels slowly decreases. This indicates partial volume effects that could be the result of voxels composed of iron corrosion products either mixed with a Ca-rich binder matrix or with porosity. Actually, both types of mixed voxels are found. The presence of voxels containing both Fe and Ca can be

inferred from the visualization of the phases in the CT images (see image in Fig. 8) and is also confirmed by chemical mapping: while iron-rich zones and Ca-rich zones are principally distinct, there are some regions where the two elements overlap (see upper left corner of Ca and Fe mapping in Fig. 2). The presence of voxels containing both Fe and porosity agrees with both lab and synchrotron CT images, where highly micro- and nanoporous iron corrosion products could be found in the TM (Fig. 7(1) and (2), respectively). While some of this porosity can be correctly handled, part of it which is nanoscale is segmented as *Iron*.

Therefore, while the major part of iron corrosion products precipitates within the sub-milliporosity of the binder, it also makes use of more indirect micro- and nano-routes, such as micro-interstices within grain binders and nanoporosity of the binder matrix. The multiscale porosity of the binder surrounding the metallic object is thus a determining factor in the corrosion process. When the amount of porosity is insufficient or it is hardly accessible, this flexible reservoir of free-space for corrosion products is lacking and stress-induced macro cracks might occur. The tortuosity of the binder's macroporous network and its related transport efficiency are also factors that influence the final shape, amount and distribution of the corrosion products. If the dissolved iron does not sufficiently migrate, the precipitation of the corrosion products leads to a volume increase in a restrained region of the sample. Mechanical stresses develop, eventually leading to the formation of cracks and fissures. To be further understood, these mechanisms require visualization and chemical investigation of the samples at the nanoscale coupled with statistical interpretation of the results.

Besides, iron corrosion products are themselves porous at multiple scales and their shape and level of crystallinity change with their location in the sample. This is particularly visible on synchrotron data, with well-crystallized iron closer to the DPL compared to the porous iron corrosion products observed in the TM (Fig. 7). This shows that the corrosion products reorganize themselves in the TM after the first precipitation step, to become thermodynamically more stable, *i.e.* more crystalline phases. Thus, our observation suggests that the clogging of porosity in the binder takes place in two steps. The first one consists of the precipitation of iron corrosion products when the solution filling the pores becomes supersaturated in iron. In the second step, when new closed pores are formed by local clogging, new well crystallized phases start to precipitate on the pore surfaces.

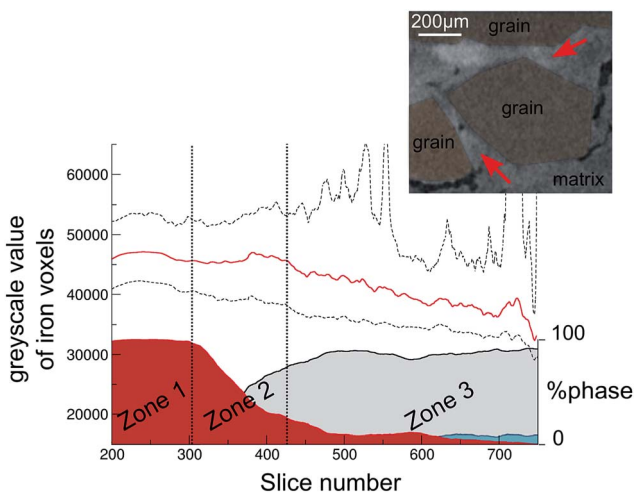


Fig. 8 Mean greyscale values (red curve) and 60% confidence margins (black dashed curves) for the iron phase in Zone 1 of the DPL and Zones 2 and 3 of the TM. The distribution of *Iron* (red), *Binder* (grey) and *Porosity* (blue) is also visualized. Inset: CT image showing diffuse boundaries between iron-rich zones and the binder matrix. This is likely to be the result of partial volume effects.

## 5 Conclusions

The procedure combining multiscale X-ray tomography, image processing and chemical data was found particularly powerful in investigating the corrosion process and its relationship with porosity. In particular, the dual use of lab tomography data with medium resolution to catch a large portion of the sample and get an overview of the relationship between the phases, and synchrotron data to dive into a detailed analysis of the phases was particularly fruitful to highlight the multiple roles of the porosity in these types of samples: sub-milliporosity, micro- and nanoporosity of the binder allow the precipitation of corrosion products and dampens the mechanical stress that could be induced during iron precipitation. The corrosion products are themselves highly porous and undergo recrystallization in the vicinity of left-over porous cavities.

Therefore, the role of porosity evolves not only with the dimension scale (from binder's nanoporosity to macro-cracks), but also with time: submilli- micro- and nanoporosity disappears by being filled with corrosion products; new porosity shows up within the precipitated corrosion phases; porosity transforms during recrystallization of the corrosion products; porosity emerges when too high mechanical pressure induces cracks and fractures. Along with this ever evolving porosity, percolation properties and transport phenomena mature with the sample.

Porosity, transport properties and corrosion processes are thus intrinsically linked. This paper is a first attempt to demonstrate that the study of their relationships is not only relevant but also necessary to better understand and predict long-term corrosion processes.

## Acknowledgements

The authors would like to acknowledge the CNRS program NEEDS Mipor for funding, the ID19 beamline staff at ESRF for their help in acquiring synchrotron X-ray data, and Anders Kaestner for sharing his image filtering software. Claire Gervais thanks the Swiss National Science Foundation for the SNF Professorship grant no. 138986.

## References


1 P. Dillmann, P. Bernardi and P. Fluzin, *Revue d'archéométrie*, 2004, 183–192.
2 L. Bertolini, M. Carsana and E. Redaelli, *J. Cult. Herit.*, 2008, **9**, 376–385.
3 G. S. Duffó, W. Morris, I. Raspini and C. Saragovi, *Corros. Sci.*, 2004, **46**, 2143–2157.
4 E. Marie-Victoire, E. Cailleux and A. Texier, *J. Phys. IV*, 2006, **136**, 305–318.
5 D. Neff, E. Marie-Victoire, V. L'Hostis, E. Cailleux, L. Vincent, A. Texier, L. Bellot-Gurlet and P. Dillmann, *Metal'07*, 2007, 30–35.
6 W.-J. Chitty, P. Dillmann, V. L'Hostis and C. Lombard, *Corros. Sci.*, 2005, **47**, 1555–1581.
7 V. L'Hostis, D. Neff, L. Bellot-Gurlet and P. Dillmann, *Mater. Corros.*, 2009, **60**, 93–98.
8 A. Demoulin, C. Trigance, D. Neff, E. Foy, P. Dillmann and V. L'Hostis, *Corros. Sci.*, 2010, **52**, 3168–3179.
9 *Advanced tomographic methods in materials research and engineering*, ed. J. Banhart, Oxford University Press, New York, 2008.
10 S. R. Stock, *Microcomputed tomography: methodology and applications*, CRC Press; Taylor and Francis, 2008.
11 L. Feldkamp, L. Davis and J. Kress, *J. Opt. Soc. Am. A*, 1984, **1**, 612–619.
12 A. Mirone, E. Brun, E. Gouillart, P. Tafforeau and J. Kieffer, *Nuclear Instruments and Methods in Physics Research Section B: Beam Interactions with Materials and Atoms*, 2014, vol 324, pp. 41–48.
13 L. I. Rudin, S. Osher and E. Fatemi, *Phys. D*, 1992, **60**, 259–268.
14 M. Burger, G. Gilboa, S. Osher and J. Xu, *Comm. Math. Sci.*, 2006, **4**, 179–212.
15 A. Kaestner, E. Lehmann and M. Stampanoni, *Adv. Water Resour.*, 2008, **31**, 1174–1187.
16 N. Otsu, *IEEE Trans. Syst. Man Cybern.*, 1979, **9**, 62–66.
17 J. Hoshen and R. Kopelman, *Phys. Rev. B: Solid State*, 1976, **14**, 3438–3445.
18 K. Tuutti, *Corrosion of Steel in Concrete*, Swedish Cement and Concrete Research Institute, 1982, pp. 6–15.